https://doi.org/10.5194/ms-2026-188
Preprint. Discussion started: 12 November 2026
© Author(s) 2026. CC BY 4.0 License.



mechanical sciences
DISCUSSIONS

Effects of Sand and Dust Particles on Tooth Surface Wear in Wind Turbine Gears

Zhongpo Hu[1],Quanwei Cui[1],*Jianxing Zhou[1],Hanxin Zhou[1]

1 School of Mechanical Engineering, Xinjiang University, Urumqi 830047, Xinjiang, China

Correspondence to: Quanwei Cui (link_cui@163.com)

Abstract: Sand and dust particles entering gear meshing interfaces induce abrasive wear, yet whether frictional responses reflect particle-size-dependent wear severity remains unclear. Wear tests on 18CrNiMo7-6 steel compared particle-free contact with three particle-size ranges (0-30μm, 30-60μm, and 60-100 μm). Friction coefficients and wear volumes were measured, and worn surfaces were characterized using three-dimensional topography, scanning electron microscopy (SEM), and energy-dispersive X-ray spectroscopy (EDS). Experimentally determined wear coefficients were incorporated into a dynamic Archard model to predict tooth surface wear distributions. Compared with the particle-free group, the mean friction coefficient and wear volume increased by 33.3-70.1% and 35.9-86.8%, respectively. From 0-30 to 60-100μm, the mean friction coefficient increased by 27.6%, whereas wear volume decreased by 27.2%. The finer particles exhibited pronounced grooving and lateral wear-track expansion, while coarser particles showed greater wear debris accumulation and residual Si and O. Under identical dynamic loading and sliding conditions, predicted wear was minimal near the pitch point. High-wear regions occurred on the approach side of the driving gear and the recess side of the driven gear, and wear peaks did not coincide with contact pressure peaks. These findings support gear wear risk assessment, wear-resistant design, and service reliability in sand- and dust-laden environments.

Keywords: Wind turbine gears; Particle size; Abrasive wear; Tooth surface wear

1 Introduction

Gearboxes are critical components of wind turbine drive trains, and their operational reliability directly affects power transmission efficiency and service performance. Tooth surface wear not only alters tooth profile geometry and contact conditions but may also affect mesh stiffness, dynamic loads, and transmission stability (Feng et al., 2023). Wind turbine gearboxes typically rely on lubricating oil and sealing systems to ensure reliable operation. The condition and contamination control of lubricating oil during long-term service directly influence the tribological performance of gear contacts (Liu et al., 2025). In wind farms frequently exposed to sand and dust, external particles can readily enter gear contact interfaces due to seal degradation, maintenance operations, or lubricant contamination. Qin et al. (2024) investigated the effects of quartz (SiO_2) particles on the tribological properties of industrial gear oils and the wear behavior of gear friction pairs. Yuan et al. (2022) examined the influence of hard third-body particles on tooth surface damage in wind turbine gears through gear tests involving Al_2O_3 abrasives. Quartz (SiO_2) particles exhibit relatively high hardness, and variations in their size and contact conditions may further influence material removal from tooth surfaces. Therefore, investigating the effects of sand and dust particles on tooth surface wear is essential for understanding the wear risks associated with gear transmission systems operating in sand- and dust-laden environments.

When sand and dust particles enter a frictional interface, their abrasive action is governed not only by particle hardness but also by the combined effects of particle size, shape, number, and contact conditions. Variations in particle size alter the geometric interference between abrasive particles and the counterface, interfacial load sharing, and particle motion, giving rise to different interaction modes, including rolling, sliding, ploughing, and cutting. Previous studies have investigated the geometric and mechanical characteristics of quartz sand particles (Blau et al., 2023), surface damage induced by third-body particles (Lan et al., 2017), and the effects of particle size distribution, counterface materials, and contact boundary conditions on wear coefficients and frictional responses (Esteves et al., 2021; Qin et al., 2019). Furthermore, the degree of particle indentation and local contact conditions are closely associated with the ploughing-to-cutting transition (Capozza and Hanley, 2024), while sustained interactions with third-body particles can lead to the evolution of surface roughness (Garcia-Suarez et al., 2024) and changes in interfacial frictional conditions (Alavi et al., 2026). These studies have demonstrated the significant influence of particle size and contact conditions on friction and wear behavior. However, differences in material systems, particle supply methods, and contact configurations among existing studies make it difficult to establish a consistent relationship between particle size, frictional resistance, and material removal. In particular, under equal-mass particle supply conditions, an increase in particle size is generally accompanied by a reduction in particle number, which may alter the probability of particles entering the contact zone, their effective load-bearing behavior, and the resulting material removal. Therefore, an increase in particle-induced frictional resistance does not necessarily correspond to a proportional increase in material removal. Controlled experiments are thus needed to further clarify the friction and wear responses and associated surface damage characteristics under different particle size conditions.

Meanwhile, tooth surface wear is governed not only by interactions between the material and abrasive particles but also by the combined effects of dynamic loading and local rolling–sliding conditions during gear meshing. As contact

https://doi.org/10.5194/ms-2026-188
Preprint. Discussion started: 12 November 2026
© Author(s) 2026. CC BY 4.0 License.



mechanical sciences
DISCUSSIONS

curvature, load sharing between meshing tooth pairs, and relative sliding velocity vary continuously along the line of action, material removal from tooth surfaces exhibits pronounced spatial nonuniformity. To account for this behavior, tooth surface wear prediction based on Archard's wear theory has progressively evolved from quasi-static contact analysis (Bajpai et al., 2004) to local wear calculations incorporating dynamic effects (He et al., 2022). Previous studies have further demonstrated the dependence of the wear coefficient on material conditions, contact loads, and lubrication conditions (Brandão et al., 2016). Dynamic gear wear prediction methods have also been refined by incorporating dynamic mesh forces, time-varying mesh stiffness, tooth-pair load sharing, and tooth surface geometry evolution (Dong et al., 2023; Walker et al., 2022; Zhang et al., 2026). However, existing studies have primarily focused on wear distributions and evolution under dynamic gear contact conditions, while particle-size-dependent differences in material removal induced by third-body particles and their quantitative incorporation into tooth surface wear predictions remain insufficiently explored. Therefore, it is necessary to integrate particle-dependent wear responses with dynamic gear contact analysis to clarify the influence of wear coefficients associated with sand and dust particles on tooth surface wear severity and characterize the spatial wear distribution under the combined effects of dynamic loading and local sliding.

Based on the above analysis, wear tests were conducted on 18CrNiMo7-6 gear steel under identical experimental conditions using different particle-size groups. The friction coefficient, wear volume, and equivalent wear coefficient were compared, with particular emphasis on whether friction and wear exhibit consistent responses to variations in particle size. The corresponding surface wear characteristics were further examined using three-dimensional surface topography, cross-sectional profiles, and scanning electron microscopy coupled with energy-dispersive X-ray spectroscopy (SEM/EDS). On this basis, the Archard wear coefficients for different particle-size groups were calibrated using the measured wear volumes. By integrating time-varying mesh stiffness, a six-degree-of-freedom gear dynamic model, and local contact and sliding analyses, a relationship was established between experimentally determined wear parameters and local tooth surface wear calculations, enabling the prediction of wear depth distributions on the driving and driven gears under different particle conditions. Furthermore, dynamic and quasi-static loading conditions were compared to investigate how dynamic mesh loads modulate local wear-driving conditions and spatial wear distributions. This study aims to reveal the distinct effects of particle size on frictional resistance and material removal under specified sand supply conditions, clarify the relationship between experimentally calibrated wear parameters and dynamic tooth surface wear distributions, and provide a reference for comparative wear assessment and engineering prediction of gear tooth surface wear induced by sand and dust particles.

2 Experimental Methods

2.1 Research Framework

The research framework is illustrated in Fig. 1. The gear dynamics analysis sequentially determines the time-varying mesh stiffness, elastic load sharing, and six-degree-of-freedom system response, yielding the dynamic normal loads acting on each active tooth pair and the instantaneous angular velocities. Based on the local involute geometry, the nominal Hertzian contact half-width, mean contact pressure, and sliding distances experienced by material points on the driving and driven gears are calculated. In the wear experiments, the friction coefficient, wear volume, and surface morphology are characterized for groups S0-S3 using the same specimen material under fixed macroscopic test conditions, and the wear coefficient K_s is calibrated. Finally, K_s is incorporated into the local Archard wear model as a scaling factor to obtain the wear depth distribution along the tooth profile.

https://doi.org/10.5194/ms-2026-188
Preprint. Discussion started: 12 November 2026
© Author(s) 2026. CC BY 4.0 License.



mechanical sciences
DISCUSSIONS

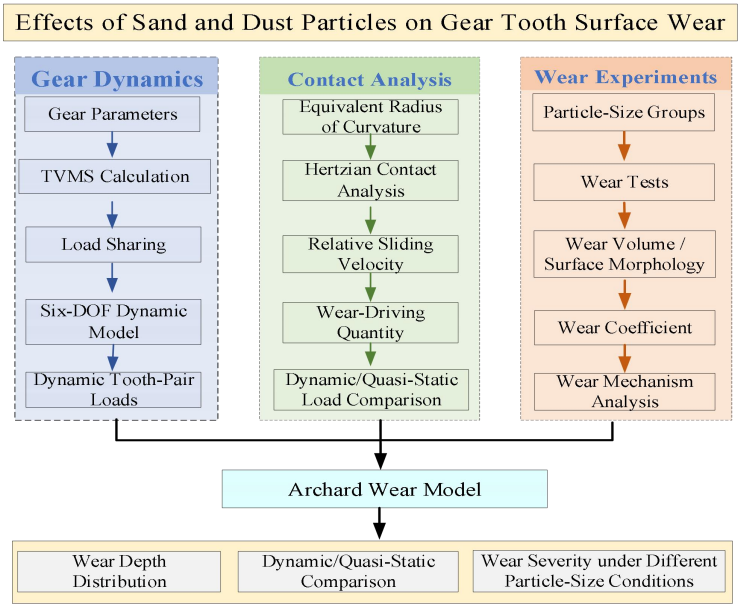


Fig. 1. Research framework.

2.2 Experimental Setup and Materials

Wear tests were conducted using an MFT-5000 multifunctional tribometer (Rtec Instruments, USA) in a linear reciprocating ball-on-flat contact configuration. The experimental configuration followed the basic arrangement specified in ASTM G133-22 for linear reciprocating ball-on-flat wear tests, with a controlled quantity of third-body particles additionally introduced to meet the research objectives. The experimental setup consisted of a normal loading unit, a reciprocating motion platform, a friction force measurement unit, and a data acquisition system, enabling real-time recording of the friction force and friction coefficient throughout the tests. All experiments were performed at room temperature under dry ambient conditions to minimize the influence of environmental fluctuations on experimental repeatability.

The flat specimens were fabricated from 18CrNiMo7-6 gear steel, the same material used for the gears under investigation, and subjected to carburizing heat treatment. Before testing, the specimen surfaces were sequentially ground using silicon carbide abrasive papers ranging from 60 to 2000 grit, followed by fine polishing with 2.5 μm polycrystalline diamond powder. After ultrasonic cleaning in absolute ethanol and thorough drying, the initial surface topography was measured using a three-dimensional profilometer. The surface roughness (Ra) ranged from 0.4 to 0.6 μm, and the surface hardness was 58 HRC. A GCr15 steel ball with a diameter of 9 mm was used as the counterbody. For each test, either a new steel ball was used or a previously unused contact region on the ball surface was selected. Each test condition was repeated three times, and the friction coefficient and wear volume were reported as mean ± standard deviation.

Commercially available SiO_2 particles were selected as abrasive particles to simulate hard particulates in sand- and dust-laden environments. The particles were supplied by Henan Changtai Materials Co., Ltd., China, with a SiO_2 content of ≥95%, a Mohs hardness of approximately 7, and a density of approximately 2.65 $g \cdot cm^{-3}$. Based on their nominal particle sizes, the abrasives were classified into three groups: S1 (0–30 μm), S2 (30–60 μm), and S3 (60–100 μm). A particle-free dry-sliding condition (S0) was established as the two-body wear control, as summarized in Table 1. The particle fractions were obtained using standard sieves, with each group distinguished by its nominal particle-size range. Before testing, the particles were dried at 120 °C for 2 h and subsequently stored in sealed containers to minimize the effects of moisture absorption and agglomeration on experimental repeatability.

Table 1 Particle size groups

Group	Particle size range (μm)	Description
S0	No particles	Dry-sliding control group
S1	0-30	Fine-particle group
S2	30-60	Medium-particle group
S3	60-100	Coarse-particle group

https://doi.org/10.5194/ms-2026-188
Preprint. Discussion started: 12 November 2026
© Author(s) 2026. CC BY 4.0 License.

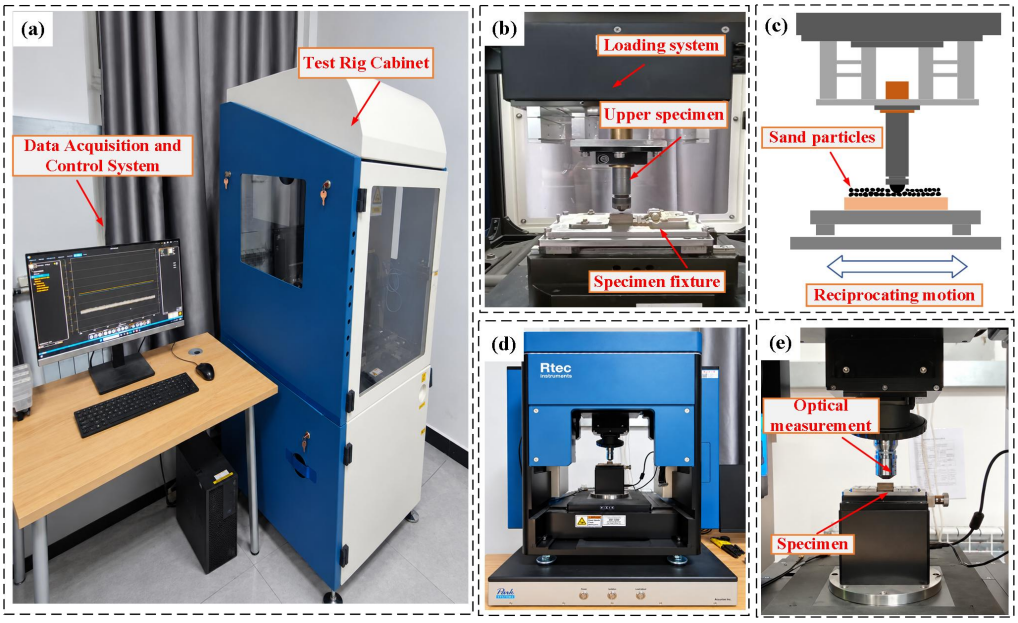


Fig. 2. Experimental environment, test equipment, and schematic illustration of the wear test.

2.3 Experimental Design

The experiments were designed to compare the effects of particle size under controlled conditions. Frictional behavior and material removal were evaluated for different particle-size groups using the same specimen material and macroscopic test conditions, and relative wear coefficients were determined for subsequent tooth surface wear prediction. A normal load of 30 N was selected primarily to produce reliably measurable wear tracks while ensuring comparability among particle-size groups under identical contact conditions. Therefore, the experimentally determined wear coefficients were primarily used to characterize the relative influence of SiO_2 particle size on wear behavior and were subsequently incorporated into the tooth surface wear model.

The tests employed a 9 mm-diameter GCr15 steel ball in point contact with a flat 18CrNiMo7-6 specimen, yielding an initial nominal Hertzian contact radius of

$$a = \left(\frac{3F_N R_b}{4E^*_{MFT}} \right)^{1/3} \tag{1}$$

The mean and maximum Hertzian contact pressures within the contact region were

$$\begin{cases} \overline{p}_M = \dfrac{F_N}{\pi a^2} \\ p_{0,M} = \dfrac{3F_N}{2\pi a^2} = \dfrac{3}{2}\overline{p}_M \end{cases} \tag{2}$$

At a normal load of 30 N, the Hertzian contact parameters obtained from Eqs. (1) and (2) characterize only the initial nominal contact state of the smooth ball-on-flat interface. As the wear track develops and abrasive particles enter the contact region, the actual load-bearing area and contact pressure distribution continuously evolve. Therefore, these nominal values should not be used to infer the actual load-bearing conditions of particles within the contact zone. The experimentally determined wear coefficient reflects the average material removal behavior over the entire test.

In the reciprocating tests, the one-way stroke length between the two reversal points is denoted by L, and the reciprocating frequency by f. The mean sliding speed and cumulative sliding distance are then expressed as follows, respectively:

$$\overline{v}_{MFT} = 2Lf, \quad S = 2Lft \tag{3}$$

The reciprocating tests were conducted at a frequency of 2 Hz, with a one-way stroke length of 10 mm and a test duration of 30 min. Before each test, 0.03 g of SiO_2 particles was weighed and uniformly distributed over the designated reciprocating wear track region. During reciprocating motion, the particles were entrained into, retained within, or expelled from the contact zone, resulting in a time-varying number of effective particles within the contact region. All groups were tested under identical conditions in terms of normal load, stroke length, test duration, particle mass, and particle distribution area. The same specimen mounting and test initiation procedures were also followed to isolate the

https://doi.org/10.5194/ms-2026-188
Preprint. Discussion started: 12 November 2026
© Author(s) 2026. CC BY 4.0 License.



mechanical sciences DISCUSSIONS

effects of particle size. Under equal-mass conditions, smaller particles correspond to a larger particle population. Differences in particle number, probability of entering the contact zone, number of load-bearing particles, and particle fragmentation behavior arising from variations in particle size were therefore considered integral components of the particle-size effect. Accordingly, the wear coefficient is defined as follows:

$$K_s = \frac{V}{2F_N Lft} \tag{4}$$

This expression characterizes the macroscopic material removal from specimens under different particle-size conditions. Since the normal load, stroke length, reciprocating frequency, and test duration were identical across all groups, the wear coefficient K_s is proportional to the wear volume, and both exhibit the same ranking across particle-size groups. This parameter provides an integrated measure of material removal efficiency associated with three-body abrasive wear under the specified material properties, contact pressure, and sliding conditions. It also serves as an experimentally calibrated parameter for subsequent tooth surface wear predictions under different particle-size conditions.

After testing, the wear track surface topography was measured using a three-dimensional profilometer. The measurement area was selected to fully cover the wear track and the unworn reference surfaces on both sides. The measured topography was sequentially processed through outlier removal, tilt correction, and reference plane fitting. Let Ω_w denote the wear track integration region, $z(x, y)$ the measured surface height after wear, and $z_{\mathrm{ref}}(x, y)$ the reference plane fitted from the surrounding unworn regions. The material removal volume can then be expressed as:

$$V_ = \iint_{\Omega_w} \max[z_{\mathrm{ref}}(x,y) - z(x,y), 0]\mathrm{d}A \tag{5}$$

The quantity $V_$ is defined as the apparent wear volume and is used to compare the extent of geometric damage to the wear tracks and calibrate the corresponding effective wear parameters. The volume of local surface protrusions above the reference plane is calculated separately as follows:

$$V_+ = \iint_{\Omega_p} \max[z(x,y) - z_{\mathrm{ref}}(x,y), 0]\mathrm{d}A \tag{6}$$

Local surface protrusions above the reference plane were characterized separately as supplementary information. In calculating the wear volume, only the material loss below the reference plane was integrated, while the volume of material piled up along the sides of the wear track was quantified separately and was not subtracted from the material removal volume. Three representative cross-sections were selected along the length of each wear track, and the maximum wear depth and wear track width were determined from the corresponding cross-sectional profiles. Multiple cross-sections from the same wear track were used to characterize variations in wear along its length and were not treated as independent experimental replicates.

3 Dynamic Gear Contact and Wear Calculation

To investigate the effects of sand and dust particle size on tooth surface wear distributions, an analytical model integrating time-varying mesh stiffness, gear dynamics, local contact analysis, and wear calculations was established. A spur gear pair was considered, with the gear material assumed to be homogeneous, isotropic, and linearly elastic. The load distribution was assumed to be approximately uniform across the tooth face width, and local contact behavior was evaluated using a nominal Hertzian elastic contact model. The gear pair parameters are listed in Table 2. Wear-induced changes in tooth profile geometry and their feedback effects on mesh stiffness were not considered. Other failure modes, including pitting, scuffing, and tooth-root fatigue, were also excluded from the scope of this study.

Table 2. Gear pair and dynamic parameters

Parameter	Driving gear	Driven gear	Unit
Number of teeth	31	96	—
Module	4	4	mm
Pressure angle	20	20	°
Face width	40	40	mm
Mass	3.603	34.658	kg
Mass moment of inertia	0.0066	0.6057	kg·m²
Support stiffness in the x-direction	5.0×10^8	5.0×10^8	N/m
Support stiffness in the y-direction	3.5×10^8	3.5×10^8	N/m
Input speed/torque	2000 r/min,128 N·m		

3.1 Time-Varying Mesh Stiffness and Load Sharing

Time-varying mesh stiffness (TVMS) is a key parameter governing the dynamic response of gear systems. Its periodic variation affects tooth-pair load sharing, dynamic normal mesh forces, and local contact conditions. The potential energy method (Wu et al., 2008) is employed to calculate the direct tooth compliance. The common gear-body

https://doi.org/10.5194/ms-2026-188
Preprint. Discussion started: 12 November 2026
© Author(s) 2026. CC BY 4.0 License.



mechanical sciences DISCUSSIONS

coupling approach proposed by Xie et al. (2018a) is further adopted to account for the influence of elastic deformation interactions between adjacent load-bearing teeth in the double-tooth meshing region. Each gear tooth is modeled as a cantilever beam with a variable cross-section, considering bending, shear, axial compression, tooth foundation deformation, and local Hertzian contact deformation. The bending, shear, and axial compression compliances are calculated using the classical potential energy method (Xie et al., 2018b), while the tooth foundation compliance is determined using the analytical model proposed by Sainsot et al. (2004). The local contact compliance is represented by the equivalent stiffness derived from classical Hertzian line contact theory. Based on the superposition of these deformation components, the total direct compliance of the r th load-bearing tooth pair at meshing phase φ is expressed as:

$$C_{rr}(\varphi)=\sum_{\ell=p,g}\left(C_{b,r}^{(k)}+C_{s,r}^{(k)}+C_{a,r}^{(k)}+C_{f,rr}^{(k)}\right)+C_{H,r} \tag{7}$$

where the superscripts p and g denote the driving and driven gears, respectively;C_b、 C_s、 C_a, and C_f represent the bending, shear, axial compression, and tooth foundation compliances, respectively; and C_H denotes the local Hertzian contact compliance. Each compliance component is calculated based on the corresponding tooth profile geometry and material properties.

In the double-tooth meshing region, adjacent load-bearing teeth undergo additional elastic deformation through their shared gear body, indicating that the tooth pairs are not mechanically independent. Following the structural coupling method proposed by Xie et al. (2018a), cross-compliance terms between adjacent tooth pairs are introduced to establish the compliance matrix for the double-tooth meshing region:

$$C_A(\varphi)=\begin{bmatrix}C_{11}(\varphi) & C_{12}(\varphi)\\ C_{12}(\varphi) & C_{22}(\varphi)\end{bmatrix}\quad C_{12}=C_{f,12}^{(p)}+C_{f,12}^{(g)} \tag{8}$$

Where C_{11} and C_{22} denote the total direct compliances of the two load-bearing tooth pairs, respectively; C_{12} represents the cross-compliance induced by the shared gear body, obtained by summing the corresponding contributions from the driving and driven gears. According to the Maxwell-Betti reciprocity theorem, the cross-compliance terms satisfy $C_{12} = C_{21}$. This cross-compliance term accounts only for the additional deformation of the shared gear body, thereby avoiding double counting of the bending, shear, and local contact compliances of individual gear teeth.

Neglecting tooth-pair manufacturing deviations and differences in local meshing clearances, the two load-bearing tooth pairs in the double-tooth meshing region undergo identical elastic approach along the common line of action. Based on the elastic deformation compatibility conditions, the overall time-varying mesh stiffness and elastic load-sharing coefficients can be expressed as follows:

$$k_m(\varphi)=1^T C_A^{-1}(\varphi)1$$
$$\beta(\varphi)=\frac{C_A^{-1}(\varphi)1}{1^T C_A^{-1}(\varphi)1} \tag{9}$$

Where1 = $[1, 1]^T$ and $\beta = [\beta_1, \beta_2]^T$ denote the elastic load-sharing vectors, which satisfy $\beta_1 + \beta_2 = 1$. In the single-tooth meshing region, the compliance matrix reduces to a single direct compliance term. Accordingly, the time-varying mesh stiffness and tooth-pair load-sharing coefficients over a complete meshing cycle can be determined. The resulting k_m is used as a time-varying parameter in the gear dynamic model, while β_r is employed to distribute the total dynamic normal mesh force among the active tooth pairs. This establishes the relationship between mesh stiffness, elastic load transfer, and dynamic local contact conditions.

3.2 Six-Degree-of-Freedom Dynamic Model of the Gear Pair

To determine the dynamic mesh loads under actual gear operating conditions, a planar six-degree-of-freedom translation–torsional coupled dynamic model was established using the lumped-parameter method, as illustrated in Fig. 3. The driving and driven gears were each modeled as rigid disks with translational and torsional degrees of freedom. The bearing and shaft supports were represented by linear spring–damper elements in two orthogonal directions, while the gear mesh was modeled using a time-varying stiffness–damping element acting along the line of action. Composite transmission error, tooth surface friction, and dynamic contact were also taken into account.

https://doi.org/10.5194/ms-2026-188
Preprint. Discussion started: 12 November 2026
© Author(s) 2026. CC BY 4.0 License.

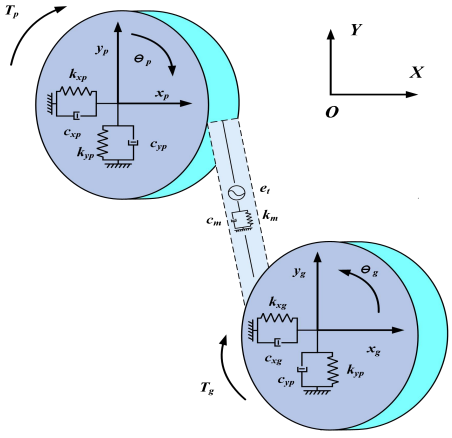


Fig. 3. Schematic illustration of the six-degree-of-freedom dynamic model, coordinate system, and mesh force directions.

With the local y axis aligned with the line of action and the local x axis aligned with the tooth-surface tangential direction, the dynamic mesh deformation is defined by considering the relative displacements of the driving and driven gears along the line of action and their torsional deformations as follows:

$$\delta(t) = \gamma^T \mathbf{q}(t) - e(t), \quad \gamma = [0, 1, r_{bp}, 0, -1, -r_{bg}]^T \tag{10}$$

Where r_{bp} and r_{bg} denote the base circle radii of the driving and driven gears, respectively; e(t) represents the composite transmission error, modeled as a periodic displacement excitation $e(t) = e_a \cos[2\pi\varphi(t) + \varphi_e]$, in which e_a and φ_e denote the transmission error amplitude and initial phase, respectively, and φ(t) is the normalized mesh phase. The calculated time-varying mesh stiffness is incorporated into the dynamic model according to the instantaneous mesh phase. Considering mesh damping and unilateral contact effects, the total dynamic normal mesh force is expressed as:

$$F_n(t) = \max\left\{0, k_m(t) g[\delta(t)] + c_m(t)\dot{\delta}(t) H[\delta(t)]\right\} \tag{11}$$

Where $g(\delta) = \max(\delta, 0)$ denotes the unilateral contact function, and $H(\delta)$ represents the contact state indicator, which equals 1 when $\delta > 0$ is satisfied and 0 otherwise; $c_m(t)$ denotes the mesh damping coefficient, calculated using $c_m(t) = 2\zeta_m \sqrt{k_m(t) m_e}$, where ζ_m is the mesh damping ratio and m_e represents the equivalent mass along the line of action. The elastic load-sharing coefficients obtained from Eq. (9) are used to approximately distribute the total dynamic normal mesh force among the active tooth pairs. The normal and friction forces acting on each tooth pair are expressed as follows:

$$\begin{aligned} F_r &= \beta_r F_n \\ F_{f,r} &= \mu_d F_r \operatorname{sgn}(v_{p,r} - v_{g,r}) \end{aligned} \tag{12}$$

Where $v_{p,r}$ and $v_{g,r}$ denote the local tangential velocities at the contact positions. The total friction force and the friction torques acting on the driving and driven gears are denoted by $F_f = \sum_r F_{f,r}$、 $M_{fp} = \sum_r F_{f,r}\rho_{p,r}$ and $M_{fg} = \sum_r F_{f,r}\rho_{g,r}$, respectively, where $\rho_{p,r}$ and $\rho_{g,r}$ represent the local radii of curvature at the corresponding contact positions. When contact is lost, the loads acting on the corresponding tooth pairs are set to zero. Based on Newton's second law of motion and the equations of rotational dynamics, the governing equations of the six-degree-of-freedom system can be expressed in a unified form as follows:

$$\begin{cases} m_p \ddot{x}_p + c_{xp}\dot{x}_p + k_{xp} x_p = F_f \\ m_p \ddot{y}_p + c_{yp}\dot{y}_p + k_{yp} y_p = -F_n \\ J_p \ddot{\theta}_p = T_p - r_{bp} F_n - M_{fp} \\ m_g \ddot{x}_g + c_{xg}\dot{x}_g + k_{xg} x_g = -F_f \\ m_g \ddot{y}_g + c_{yg}\dot{y}_g + k_{yg} y_g = F_n \\ J_g \ddot{\theta}_g = r_{bg} F_n - T_g + M_{fg} \end{cases} \tag{13}$$

To investigate the influence of differences in experimentally determined wear coefficients on tooth surface wear, a common friction coefficient μ_d was adopted in the dynamic model for all particle-size groups. Its value was set to the arithmetic mean of the experimentally measured mean friction coefficients across all groups. The equations of motion were solved using an adaptive Runge–Kutta method. After eliminating the initial transient response, the steady-state tooth-pair loads and angular velocities were extracted and mapped onto discrete nodes along the tooth profile according to the meshing phase.

https://doi.org/10.5194/ms-2026-188
Preprint. Discussion started: 12 November 2026
© Author(s) 2026. CC BY 4.0 License.



mechanical sciences DISCUSSIONS

3.3 Local Contact Analysis and Tooth Surface Wear Calculation

Tooth surface wear is influenced not only by the dynamic normal load but also by local contact geometry and relative sliding between the mating tooth surfaces. To establish the relationship between dynamic mesh loads and local material removal, a nominal Hertzian line contact model is employed to calculate the local contact pressure. For standard involute tooth profiles, the local radii of curvature of the driving and driven gears at each contact node are denoted by $\rho_{p,i} = r_{bp} \tan \alpha_{p,i}$ and $\rho_{g,i} = r_{bg} \tan \alpha_{g,i}$, respectively, where $\alpha_{p,i}$ and $\alpha_{g,i}$ represent the local involute pressure angles of the corresponding tooth surfaces. The equivalent radius of curvature and effective elastic modulus of the gear pair are expressed as follows:

$$\frac{1}{R_i^*} = \frac{1}{\rho_{p,i}} + \frac{1}{\rho_{g,i}}$$
$$\frac{1}{E^*} = \frac{1-\nu_p^2}{E_p} + \frac{1-\nu_g^2}{E_g} \tag{14}$$

Assuming an approximately uniform load distribution across the tooth face width, linear elastic material behavior, and a contact region much smaller than the local radii of curvature, the instantaneous contact conditions are determined using classical Hertzian line contact theory (Xing et al., 2023). The contact half-width and mean contact pressure over the contact region are expressed as follows, respectively:

$$b_{H,i} = \sqrt{\frac{4F_{r,i}R_i^*}{\pi B E^*}}$$
$$\bar{p}_{H,i} = \frac{F_{r,i}}{2Bb_{H,i}} \tag{15}$$

where B denotes the tooth face width, b_H is the Hertzian contact half-width, $\bar{p}_H$ represents the mean contact pressure over the contact band, and F_r denotes the normal load distributed to the current load-bearing tooth pair by the dynamic model. The nominal pressure distribution within the Hertzian contact band and the corresponding local geometric relationships are illustrated in Fig. 4(a).

A single-point observation approach is adopted to calculate the relative sliding distance experienced by each tooth surface node during a single contact passage (Flodin and Andersson, 1997). The local tangential velocity is expressed as $v_{j,i} = \Omega_j \rho_{j,i}$, where $\Omega_j = \omega_{j0} + \dot{\theta}_j$ and ω_{j0} denote the instantaneous and nominal angular velocities, respectively. Assuming that the normal load, local curvature, and tangential velocity remain approximately constant during a single contact passage, the relative sliding distances experienced by the corresponding nodes on the driving and driven gears can be expressed as follows, respectively:

$$s_{p,i} = 2b_{H,i} \frac{|v_{p,i} - v_{g,i}|}{|v_{p,i}|}$$
$$s_{g,i} = 2b_{H,i} \frac{|v_{p,i} - v_{g,i}|}{|v_{g,i}|} \tag{16}$$

Therefore, the sliding distance experienced during a contact passage depends not only on the contact band width but also on the local rolling–sliding kinematics.

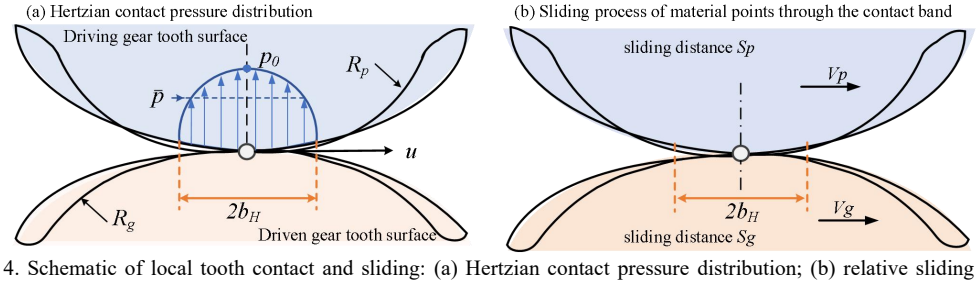


Fig. 4. Schematic of local tooth contact and sliding: (a) Hertzian contact pressure distribution; (b) relative sliding of tooth surface material points.

To describe tooth surface material removal induced by sand and dust particles, the Archard wear model is employed to establish the relationship between normal contact loading, relative sliding distance, and wear depth (Brandão et al, 2016) in material removal efficiency among particle-size groups are represented by the equivalent wear coefficient K_s, calibrated from the wear experiments using Eq. (4). Under the mean contact pressure approximation and the linear Archard wear relationship, the incremental wear depth experienced by a material point during a single passage through the contact band is expressed as $\Delta h_{j,i} = K_s \bar{p}_{H,i} S_{j,i}$ .Substituting Eqs. (15) and (16) yields:

https://doi.org/10.5194/ms-2026-188
Preprint. Discussion started: 12 November 2026
© Author(s) 2026. CC BY 4.0 License.



mechanical sciences DISCUSSIONS

$$\Delta h_{j,i} = K_s \frac{F_{r,i}}{B} \frac{|v_{p,i} - v_{g,i}|}{|v_{j,i}|} \tag{17}$$

Equation (17) indicates that, under the mean contact pressure approximation and the assumption of constant velocity during contact, the Hertzian contact half-width cancels out in the product of contact pressure and sliding distance. Consequently, the wear depth per contact passage is jointly determined by the dynamic normal load per unit face width, local rolling–sliding kinematics, and the equivalent wear coefficient. Nevertheless, contact geometry and material elastic properties continue to influence the predicted wear through their effects on mesh stiffness and dynamic loads.

To facilitate the analysis of the influence of dynamic loading on local wear, a wear-driving quantity $D_{j,i} = (F_{r,i} / B)\left|v_{p,i} - v_{g,i}\right| / \left|v_{j,i}\right|$ is defined to characterize the driving effect on material removal arising from the combined contributions of the normal load per unit face width and local rolling–sliding kinematics. During the initial wear stage, when wear-induced changes in tooth surface geometry and load distribution remain negligible, the wear depth increments associated with successive meshing cycles are assumed to accumulate linearly. Accordingly, the cumulative wear depth can be expressed as follows:

$$h_{j,i} = N_j \Delta h_{j,i} = N_j K_s D_{j,i} \tag{18}$$

For identical gear parameters and dynamic inputs, $D_{j,i}$ characterizes the spatial distribution arising from the combined effects of contact loading and local sliding, whereas the equivalent wear coefficient K_s accounts for differences in wear behavior among the particle-size groups under the experimental conditions. The application of experimentally calibrated wear coefficients to tooth surface wear calculations represents a conditional parameter transfer, whose applicability is constrained by the contact configuration, kinematic conditions, and particle supply conditions.

4 Results and Discussion

4.1 Effects of Particle Size on Friction and Wear

Figure 5 presents the temporal evolution of the friction coefficient and its mean value for each group. The particle-free group (S0) exhibited a relatively low friction coefficient, whereas the addition of particles increased the friction coefficient across all particle-size groups. The mean friction coefficients for groups S0–S3 were 0.378, 0.504, 0.581, and 0.643, respectively, corresponding to increases of 33.3%, 53.7%, and 70.1% for the particle-containing groups compared with S0. Differences were also observed in the temporal evolution of the friction coefficient among the particle-containing groups. Group S1 exhibited a relatively stable frictional response, whereas S2 showed a decrease during the middle and later stages of the test. In contrast, S3 maintained a comparatively high friction coefficient accompanied by noticeable fluctuations. These variations suggest differences in the interfacial frictional states and their evolution among the particle-size groups. However, the friction coefficient curves alone are insufficient to determine the specific contributions of particle fragmentation, expulsion, or changes in particle coverage.

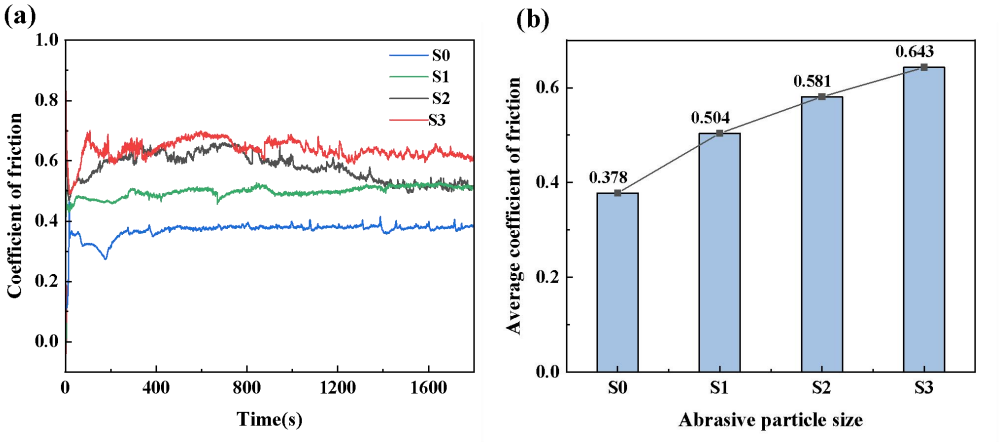


Fig. 5. Frictional responses under different particle-size conditions: (a) temporal evolution of the friction coefficient; (b) mean friction coefficient.

Figure 6 and Table 3 show that the addition of abrasive particles also increased the wear volume. The wear volumes for groups S0–S3 were 0.0515, 0.0962, 0.0766, and 0.0700 mm³, respectively, corresponding to increases of

https://doi.org/10.5194/ms-2026-188
Preprint. Discussion started: 12 November 2026
© Author(s) 2026. CC BY 4.0 License.



mechanical sciences DISCUSSIONS

86.8%, 48.7%, and 35.9% for the particle-containing groups compared with S0. Thus, relative to particle-free dry sliding, the presence of abrasive particles resulted in higher frictional resistance and larger wear track depression volumes. However, a different trend was observed when comparing the particle-containing groups. From S1 to S3, the mean friction coefficient increased from 0.504 to 0.643, whereas the wear volume decreased from 0.0962 to 0.0700 mm^3, corresponding to an increase of 27.6% and a decrease of 27.2%, respectively. The mean values of the three particle-size groups indicate that the friction coefficient increased with increasing nominal particle size, while the wear volume exhibited the opposite trend. These findings demonstrate that, under the specified contact and particle conditions, frictional resistance and apparent wear severity do not vary consistently. Therefore, the abrasive wear severity induced by particles cannot be reliably assessed based solely on the friction coefficient.

The wear track width and maximum wear depth further highlight these differences. All particle-containing groups exhibited wider wear tracks than S0, whereas the mean maximum wear depth did not increase correspondingly. Among them, S1 exhibited the largest mean wear track width and wear volume, indicating that the increased damage was primarily associated with lateral expansion of the affected region. The maximum wear depth represents a local extreme, while the wear track width and wear volume characterize the extent of surface damage and the overall geometric changes, respectively. Therefore, these three parameters should be considered together when evaluating wear severity. Since the normal load and cumulative sliding distance were identical across all groups, the equivalent wear coefficient calculated using Eq. (4) was proportional to the wear volume. Consequently, the identical ranking of wear coefficients and wear volumes is a direct result of the normalization procedure. The equivalent wear coefficient was used to characterize the wear response of each particle-size group and served as an input parameter for subsequent tooth surface wear calculations. Under equal-mass particle supply conditions, variations in particle size were accompanied by changes in particle number and the conditions governing particle entry into and retention within the contact zone. Therefore, these results characterize the effects of particle-size groups under the specified particle supply conditions, and their applicability is jointly constrained by material properties, contact configuration, and experimental conditions.

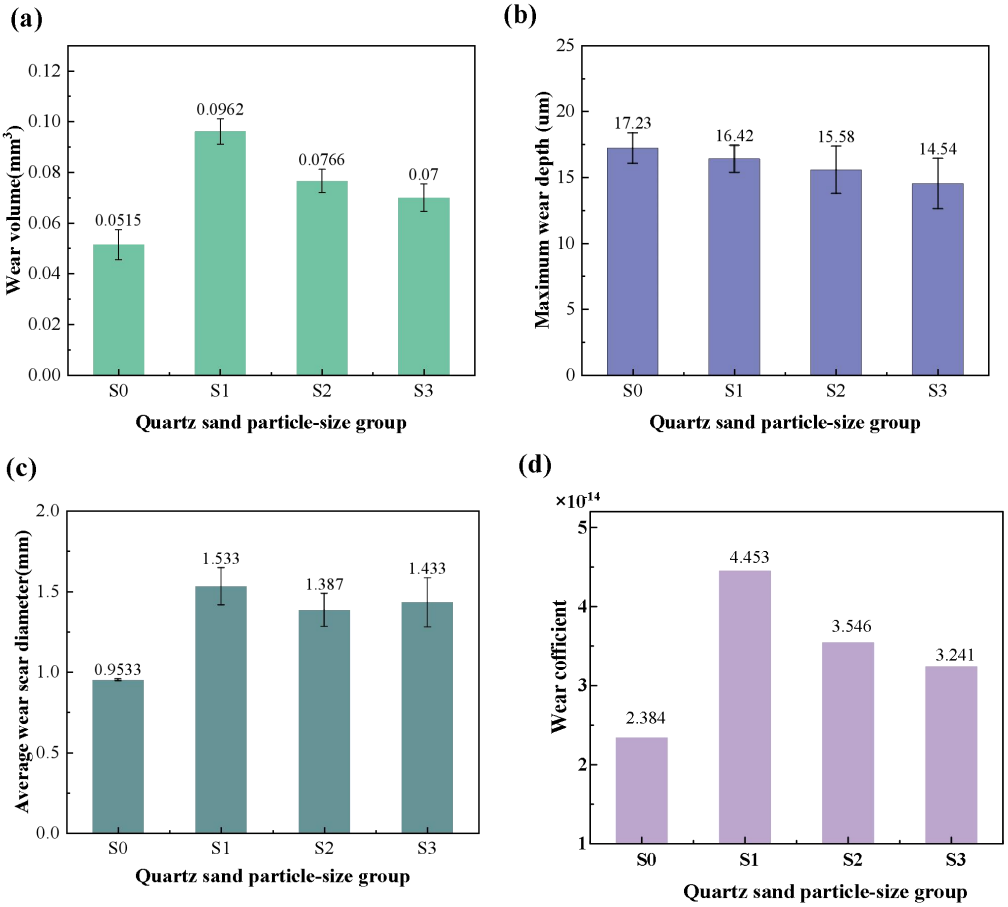


Fig. 6. Wear characteristics under different particle-size conditions: (a) wear volume; (b) maximum wear depth; (c) wear track width; (d) wear coefficient.

https://doi.org/10.5194/ms-2026-188
Preprint. Discussion started: 12 November 2026
© Author(s) 2026. CC BY 4.0 License.



mechanical sciences
DISCUSSIONS

Table 3. Summary of friction and wear results under different test conditions.

condition	mean friction coefficient	wear volume V^{-} /mm³	maximum wear depth/μm	wear track width/mm	Ks (10^{-14}m²/N)
S0	0.378	0.0515	17.23	0.953	2.384
S1	0.504	0.0962	16.42	1.533	4.453
S2	0.581	0.0766	15.58	1.387	3.546
S3	0.643	0.0700	14.54	1.433	3.241

4.2 Analysis of Wear Track Morphology and Wear Characteristics

To elucidate the differences in friction and wear responses among the particle-size groups, three-dimensional surface topography obtained by white-light interferometry, two-dimensional cross-sectional profiles, scanning electron microscopy (SEM), and energy-dispersive X-ray spectroscopy (EDS) were used to analyze wear track geometry, localized surface damage, and elemental distributions. SEM microscope images were acquired using a ZEISS EVO 15 scanning electron microscope.

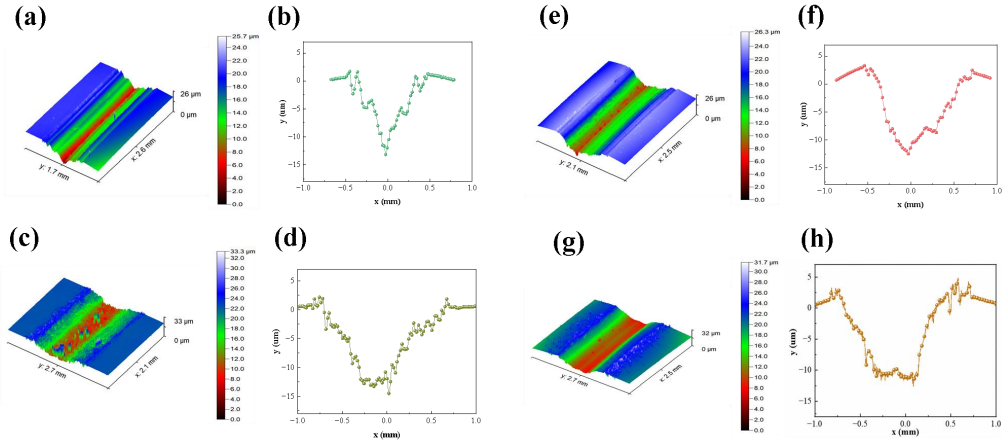


Fig. 7. Three-dimensional wear morphologies and cross-sectional profiles under different particle-size conditions: (a, b) S0; (c, d) S1; (e, f) S2; (g, h) S3.

Figure 7 presents the three-dimensional wear track morphologies and representative two-dimensional cross-sectional profiles under different particle-size conditions. As observed, the wear track of the particle-free group S0 was relatively narrow, whereas the addition of SiO_2 particles led to pronounced lateral expansion of the wear regions in all particle-containing groups. Among them, S1 exhibited a relatively wide and continuous depressed region, consistent with its larger wear volume. In contrast, the wear track surfaces of S2 and S3 showed more pronounced local undulations and geometric nonuniformity. Combined with the data in Table 3, the mean wear track width of S1 increased from 0.953 mm for S0 to 1.533 mm, while the maximum wear depth did not increase correspondingly. This indicates that the apparent enhancement of wear induced by particles was primarily manifested as lateral expansion of the wear track depression region rather than an increase in local maximum depth. The trends revealed by the two-dimensional cross-sectional profiles are consistent with those observed in the three-dimensional surface morphologies, indicating that surface damage under different particle-size conditions involved not only local groove formation but also varying degrees of plastic deformation, wear debris accumulation, and surface morphology reconstruction. Therefore, the maximum wear depth alone is insufficient to comprehensively evaluate the severity of particle-induced surface damage, and a combined analysis of wear track width and wear volume is also required.

https://doi.org/10.5194/ms-2026-188
Preprint. Discussion started: 12 November 2026
© Author(s) 2026. CC BY 4.0 License.

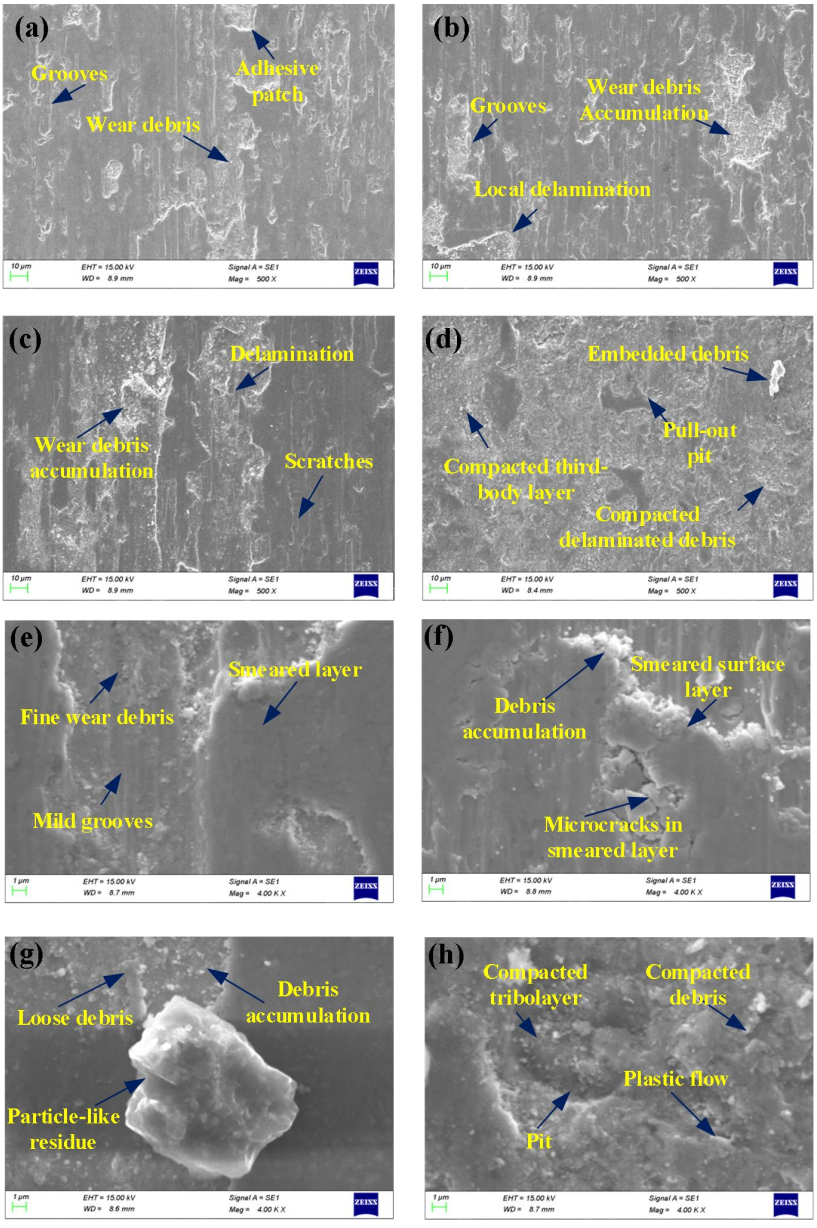


Fig. 8. SEM images of worn surfaces under different particle-size conditions: (a, e) S0; (b, f) S1; (c, g) S2; (d, h) S3. All SEM images were acquired by the authors using a ZEISS EVO 15 scanning electron microscope. These images are original experimental results obtained in the present study and have not been reproduced or adapted from previously published sources.

Figure 8 further illustrates the microscopic wear characteristics of the different particle-size groups. The worn surface of S0 was primarily characterized by shallow grooves aligned with the sliding direction, limited wear debris, and localized smearing. Fine scratches and localized deformation of the surface layer were observed at higher magnification, indicating that mild surface scratching and localized adhesive deformation were the dominant damage features under particle-free conditions. In contrast, S1 exhibited more pronounced continuous grooves, wear debris accumulation, and localized surface delamination. Fine wear debris, smeared layers, and localized microcracks were also observed at higher magnification, revealing more evident abrasive scratching and surface damage, consistent with its larger wear track width and wear volume. The worn surface of S2 exhibited grooves, scratches, and localized delamination, accompanied by granular residues and relatively large wear debris, reflecting the coexistence of localized

https://doi.org/10.5194/ms-2026-188
Preprint. Discussion started: 12 November 2026
© Author(s) 2026. CC BY 4.0 License.



mechanical sciences
DISCUSSIONS

abrasive interactions and material deformation. S3 showed more pronounced localized pits, wear debris accumulation, and compacted deposits. At higher magnification, residual particles, localized compacted layers, and plastic flow marks were observed, indicating that the worn surface under coarse-particle conditions exhibited distinct local deformation and third-body residue characteristics compared with S1. These morphological differences suggest that variations in particle size can alter local interfacial contact conditions and surface damage mechanisms. However, post-test SEM observations alone are insufficient to directly determine the rolling, fragmentation, and expulsion behavior of particles during sliding.

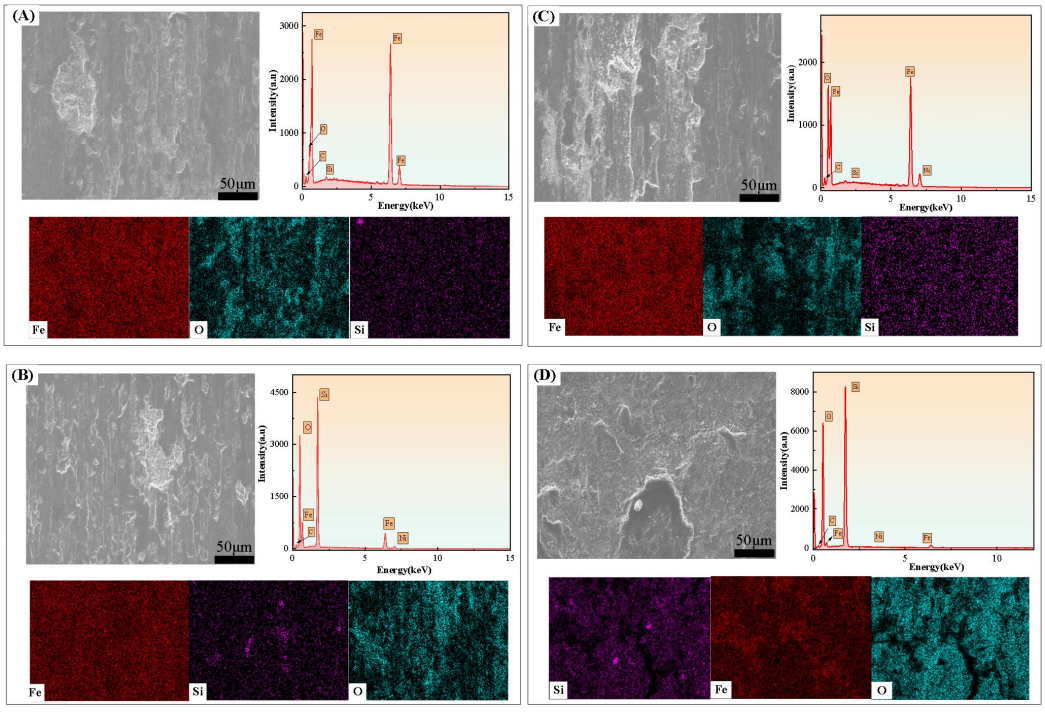


Fig. 9. SEM-EDS analysis of representative wear track regions under different particle-size conditions: (a) S0; (b) S1; (c) S2; (d) S3.

Table 4. EDS-determined mass fractions of major elements in selected regions of representative wear tracks (wt.%).

Condition	Fe/wt.%	O/wt.%	Si/wt.%
S0	92.77	3.54	0.26
S1	26.29	38.23	30.76
S2	82.58	12.97	0.23
S3	5.76	52.61	38.44

Figure 9 and Table 4 further reveal differences in the elemental distributions of the worn surfaces among the particle-size groups. The selected region in S0 was dominated by Fe, with a mass fraction of 92.77%, while the Si and O contents were only 0.26% and 3.54%, respectively, indicating predominant exposure of the steel substrate. In the selected region of S1, the Si and O contents increased to 30.76% and 38.23%, respectively, whereas the Fe content decreased to 26.29%. These results indicate substantial retention of Si- and O-containing particles or wear debris in this region, consistent with the debris accumulation and localized surface coverage observed by SEM. The selected region of S2 remained Fe-dominated, with a Si content of only 0.23%, indicating no pronounced Si enrichment in the analyzed region. However, this does not exclude the presence of residual quartz particles elsewhere along the wear track. In contrast, the Si and O contents in the selected region of S3 reached 38.44% and 52.61%, respectively, while the Fe content decreased to 5.76%. Combined with the localized compaction and surface coverage observed by SEM, these results suggest substantial accumulation of Si/O-rich third-body residues in this region. It should be noted that the EDS results reflect the elemental composition of representative analyzed regions and cannot independently determine the specific phase composition, thickness, or load-bearing capacity of the third-body layer. Furthermore, these localized measurements cannot directly represent the extent of particle coverage over the entire wear track.

Considering the wear track geometry, SEM observations, and EDS results collectively, the differences in frictional behavior and material removal among the particle-size groups are associated with combined variations in particle

https://doi.org/10.5194/ms-2026-188
Preprint. Discussion started: 12 November 2026
© Author(s) 2026. CC BY 4.0 License.



mechanical sciences DISCUSSIONS

number, local mechanical interactions, and third-body residue characteristics. Under equal-mass particle supply conditions, the fine-particle group contains a relatively larger nominal number of particles, potentially increasing the opportunities for abrasive particles to participate in interfacial scratching. Consequently, S1 exhibited more pronounced continuous grooves, wider wear tracks, and a larger apparent wear volume. As particle size increased, localized indentation by coarser particles, wear debris accumulation, and residual surface coverage could alter the interfacial shear conditions, leading to different trends in frictional resistance and material removal. This interpretation is consistent with previous findings that particle size, contact conditions, and ploughing-to-cutting behavior jointly influence wear responses (Esteves et al., 2021; Capozza and Hanley, 2024). Therefore, the increase in friction coefficient accompanied by a decrease in wear volume from S1 to S3 further indicates that interfacial tangential resistance and material removal respond differently to variations in particle size.

4.3 Dynamic Gear Meshing and Local Contact Characteristics

To elucidate the influence of dynamic gear meshing on local wear, the time-varying mesh stiffness, tooth-pair load sharing, and contact pressure and sliding characteristics along the active line of action were analyzed under the baseline operating condition. The effects of gear dynamics on the local tooth surface wear-driving quantity were further investigated by comparing dynamic and quasi-static results. Based on the geometric parameters of the gear pair and assuming standard involute gears without profile shift, the theoretical transverse contact ratio was approximately 1.75, and the nominal total normal mesh force was approximately 2.20 kN. These values provide a fundamental mechanical reference for interpreting single- and double-tooth load-bearing conditions and local load variations.

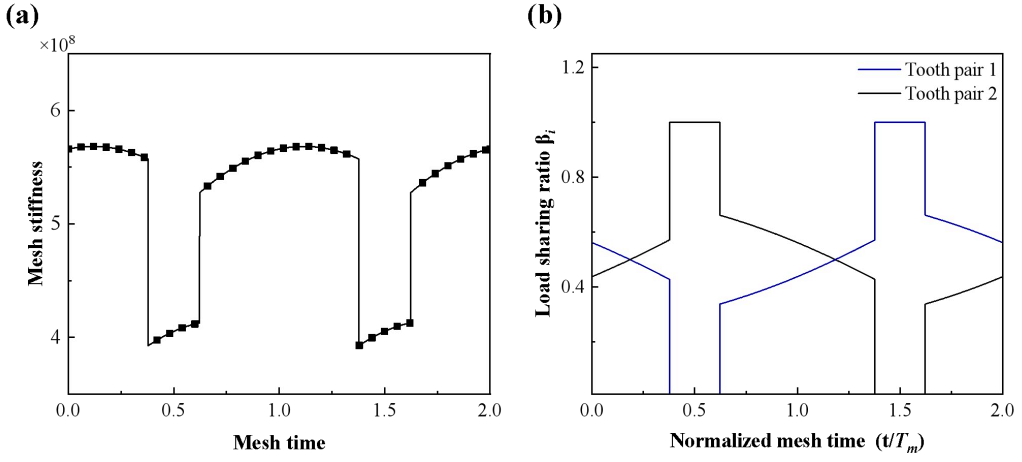


Fig. 10. Time-varying mesh stiffness and tooth-pair load-sharing characteristics of the gear pair: (a) time-varying mesh stiffness; (b) tooth-pair load-sharing coefficients.

Figure 10 illustrates the time-varying mesh stiffness and tooth-pair load-sharing characteristics of the gear pair. As shown in Fig. 10(a), the mesh stiffness exhibits pronounced periodic variations associated with the transitions between single- and double-tooth meshing regions. The mesh stiffness remains relatively high in the double-tooth meshing regions but decreases markedly in the single-tooth meshing region, with abrupt changes occurring during transitions between load-bearing tooth pairs. This behavior is primarily attributed to changes in the number of load-bearing tooth pairs, which alter the overall system compliance. In addition, tooth bending, shear deformation, tooth foundation deformation, and structural coupling through the common gear body further influence the mesh stiffness at different meshing positions. Figure 10(b) shows that the load-sharing coefficients of adjacent tooth pairs in the double-tooth meshing region are not equal but vary with the meshing position. Pronounced jumps in load sharing occur at the transitions between single- and double-tooth meshing regions. Once the gear pair enters the single-tooth meshing region, the entire normal load is carried by the active tooth pair. Previous studies have demonstrated that structural coupling through the common gear body modifies the elastic deformation compatibility between adjacent tooth pairs in the double-tooth meshing region, thereby affecting the overall mesh stiffness and load distribution (Xie et al., 2018a). The predicted periodic stiffness variations and tooth-pair load transfer characteristics are consistent with these theoretical findings in terms of their physical trends. Therefore, the dynamic normal load allocated to each active tooth pair should be used in subsequent local contact calculations to account for variations in load-bearing conditions at different meshing positions.

https://doi.org/10.5194/ms-2026-188
Preprint. Discussion started: 12 November 2026
© Author(s) 2026. CC BY 4.0 License.



mechanical sciences
DISCUSSIONS

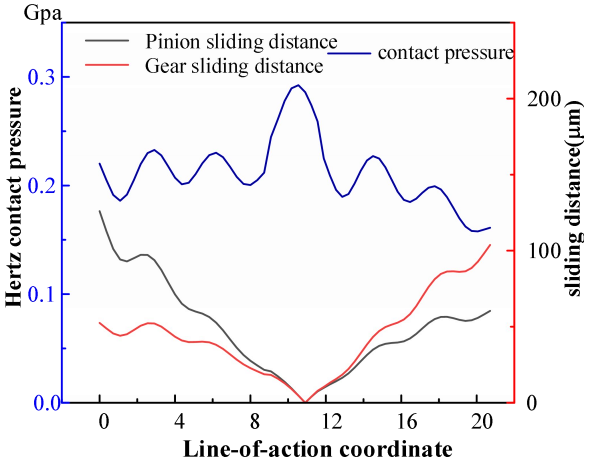


Fig. 11. Local contact pressure and sliding distances along the line of action under dynamic loading.

Figure 11 presents the mean Hertzian contact pressure and the sliding distances experienced by material points on the driving and driven gears along the active line of action. Here, the sliding distance refers to the relative sliding distance accumulated by a tooth surface material point during a single passage through the local contact band. As shown in the figure, the contact pressure exhibits a pronounced nonuniform distribution along the line of action, with relatively higher values in the single-tooth meshing region and a local peak near the pitch point. This is primarily because the entire normal load is carried by a single tooth pair in the single-tooth meshing region, while variations in local contact curvature and dynamic tooth-pair loads further modulate the contact pressure. Unlike the contact pressure, the sliding distances of both the driving and driven gears approach zero near the pitch point and gradually increase toward the approach and recess sides, although their magnitudes differ considerably on either side of the pitch point. Specifically, the driving gear exhibits a larger sliding distance on the approach side, whereas the driven gear shows a relatively larger value on the recess side. These differences are mainly attributed to variations in the local tangential velocities of the mating tooth surfaces and the residence times of material points within the contact band. Although the contact pressure is relatively high near the pitch point, the mating tooth surfaces approach an instantaneous pure rolling condition, causing the relative sliding velocity to approach zero and the local sliding distance to reach its minimum. Previous gear wear studies based on the single-point observation method and Archard wear model have demonstrated that local material removal is governed by the combined effects of contact loading and relative sliding (Bajpai et al., 2004; Ren and Yuan, 2022). Therefore, within the adopted sliding wear model, regions of high contact pressure do not necessarily correspond to regions of severe wear. The spatial distribution of tooth surface wear must be evaluated by considering both contact loading and local rolling – sliding kinematics.

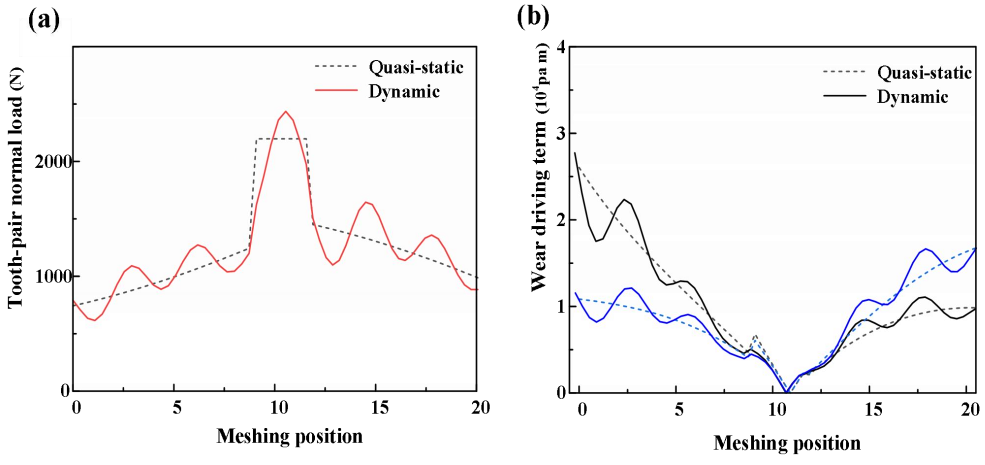


Fig. 12. Comparison of local loads and wear-driving quantities under dynamic and quasi-static conditions: (a) tooth-pair normal load; (b) wear-driving quantity.

https://doi.org/10.5194/ms-2026-188
Preprint. Discussion started: 12 November 2026
© Author(s) 2026. CC BY 4.0 License.



mechanical sciences
DISCUSSIONS

To investigate the influence of gear dynamics on local wear-driving quantities, the tooth-pair loads and wear-driving quantities under dynamic and quasi-static conditions were compared, as shown in Fig. 12. As illustrated in Fig. 12(a), the tooth-pair loads under both conditions exhibit similar overall distribution trends. However, the dynamic results show more pronounced local fluctuations at the transitions between single- and double-tooth meshing regions and within the single-tooth meshing region. The loads increase at certain meshing positions but decrease at others, indicating that dynamic effects do not simply amplify the quasi-static loads by a uniform factor. Instead, they modulate the local load-bearing conditions through time-varying mesh stiffness, load transfer, and system vibration responses. In Fig. 12(b), the black and blue curves correspond to the driving and driven gears, respectively, while the solid and dashed lines represent the dynamic and quasi-static results, respectively. The wear-driving quantities of both gears approach zero near the pitch point, whereas the dynamic results exhibit more pronounced local peaks and valleys on either side of the pitch point. Specifically, higher wear-driving quantities are primarily concentrated on the approach side of the driving gear and the recess side of the driven gear, consistent with the sliding distance distributions shown in Fig. 11. These results indicate that local rolling–sliding kinematics and tooth-pair loads jointly determine the spatial distribution of the wear-driving quantity, while dynamic loading further modulates the wear intensity at different meshing positions. This behavior is consistent with the nonuniform wear characteristics reported in previous studies incorporating dynamic mesh forces into tooth surface wear prediction (He et al., 2022; Ren and Yuan, 2022). Collectively, Figs. 10–12 demonstrate that time-varying mesh stiffness and tooth-pair load sharing influence local load-bearing conditions, while contact geometry and rolling–sliding kinematics govern variations in contact pressure and sliding distance. Dynamic mesh loads further modulate the wear-driving intensity at different positions along the tooth profile. Therefore, nonuniform sliding wear on tooth surfaces cannot be attributed solely to variations in contact pressure but arises from the combined effects of local normal loading and relative sliding. These findings provide a mechanical basis for incorporating the equivalent wear coefficients obtained under different particle-size conditions into subsequent predictions of wear depth distributions along the tooth profiles of the driving and driven gears.

4.4 Tooth Surface Wear Distributions under Different Particle-Size Conditions

The equivalent wear coefficients for groups S0–S3 listed in Table 3 were incorporated into the local Archard wear model to predict the wear depth distributions of the driving and driven gears along the active line of action under different particle-size conditions, while maintaining identical dynamic loading and sliding conditions, as shown in Fig. 13.

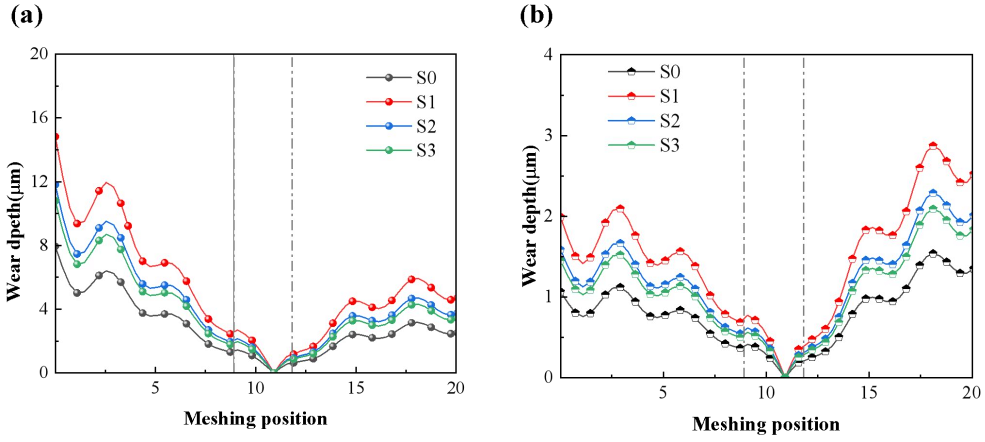


Fig. 13. Tooth surface wear distributions under different particle-size conditions: (a) driving gear; (b) driven gear.

As shown in Fig. 13, the wear depth distributions of both the driving and driven gears exhibit pronounced nonuniformity, but the regions of severe wear differ spatially. Higher wear depths are mainly concentrated on the approach side of the driving gear and the recess side of the driven gear, while the wear depths of both gears approach zero near the pitch point. Combined with Figs. 11 and 12, these distributions are consistent with the variations in local sliding distance and wear-driving quantity. Although the contact pressure is relatively high near the pitch point, the relative sliding velocity approaches zero, resulting in a substantial reduction in local sliding wear predicted by the Archard model. This indicates that the spatial distribution of tooth surface wear is not governed solely by contact pressure but arises from the combined effects of local normal loading and rolling–sliding kinematics.

The wear depth curves under different particle-size conditions exhibit similar spatial distribution patterns but differ considerably in magnitude, following the overall order S1 > S2 > S3 > S0. This trend is consistent with the experimentally measured wear volumes and equivalent wear coefficients. According to Table 3, the equivalent wear coefficients of S1, S2, and S3 are 1.868, 1.487, and 1.359 times that of S0, respectively. Under identical mechanical boundary conditions, the predicted wear depths follow the same proportional relationships. This indicates that, within

https://doi.org/10.5194/ms-2026-188
Preprint. Discussion started: 12 November 2026
© Author(s) 2026. CC BY 4.0 License.



mechanical sciences
DISCUSSIONS

the adopted linear Archard wear model, the influence of particle size on material removal is transferred to tooth surface wear predictions through the experimentally calibrated equivalent wear coefficients, while local loading and sliding conditions determine the spatial wear distribution. Therefore, the similar wear distribution patterns among the particle-size groups are a consequence of the common dynamic boundary conditions adopted in the model, rather than direct evidence that particle size has no influence on local contact conditions.

Furthermore, the overall cumulative wear of the driving gear is greater than that of the driven gear, primarily due to the combined effects of local wear-driving quantities and meshing cycle counts. Based on the tooth number ratio, each tooth of the driving gear undergoes approximately 3.10 times as many meshing cycles as each tooth of the driven gear over the same prediction period. Meanwhile, Fig. 12 indicates that the driving gear exhibits a higher local wear-driving quantity on the approach side. These two factors jointly contribute to the greater cumulative wear depth of the driving gear. This demonstrates that differences in wear between the driving and driven gears depend not only on local material removal intensity but also on the frequency of repeated contact. Overall, dynamic loading and local sliding jointly govern the nonuniform distribution of tooth surface wear, whereas the equivalent wear coefficients associated with different particle sizes primarily affect the predicted wear magnitude. Since particle-induced changes in local load-bearing conditions and wear-induced tooth profile feedback are not explicitly considered, the present results are mainly intended for comparative wear assessment among different particle-size groups under the specified conditions.

5 Conclusions

To investigate tooth surface wear under abrasive particle ingress, this study combined wear experiments with dynamic local gear contact analysis to examine the effects of particle size on the friction and wear behavior of 18CrNiMo7-6 steel and their implications for tooth surface wear distributions. The main conclusions are as follows:

(1) The presence of abrasive particles markedly increased friction and material removal. Compared with the particle-free control group, all particle-containing groups exhibited higher mean friction coefficients and wear volumes, although these two parameters showed different trends with increasing particle size. As the particle size increased from 0–30 to 60–100 μm, the mean friction coefficient increased from 0.504 to 0.643, whereas the wear volume decreased from 0.0962 to 0.0700 mm³, corresponding to an increase of 27.6% and a decrease of 27.2%, respectively. These results indicate that, under the present experimental conditions, an increase in friction coefficient does not necessarily correspond to a larger wear volume. Therefore, the severity of particle-induced wear should be evaluated by considering both frictional and wear-related indicators.

(2) The worn surfaces exhibited distinct morphological and damage characteristics under different particle-size conditions. The 0–30 μm group showed more pronounced wear track widening, continuous grooves, and localized surface delamination, whereas the 60–100 μm group exhibited more localized pits, wear debris accumulation, and residual surface coverage containing Si and O. The addition of particles generally increased the wear track width without a corresponding increase in maximum wear depth. This indicates that particle-induced surface damage involves not only localized material loss but also lateral expansion of wear tracks and changes in surface morphology. These morphological observations provide supporting evidence for explaining the distinct friction and wear responses observed under different particle-size conditions.

(3) Tooth surface wear depth exhibited a pronounced nonuniform distribution governed by the combined effects of dynamic tooth-pair loads and local sliding distances. The relatively small sliding distance near the pitch point resulted in a region of low sliding wear, while the high-wear regions of the driving and driven gears were concentrated on the approach and recess sides, respectively. This indicates that contact pressure alone is insufficient to accurately identify the locations of maximum wear. Furthermore, differences in the wear-driving quantities of the driving and driven gears contributed to variations in their cumulative wear. Under identical loading and sliding conditions across the particle-size groups, the equivalent wear coefficients primarily determined differences in the predicted wear magnitude, whereas dynamic loading and local sliding jointly influenced wear intensity and its spatial distribution.

Data availability

The data analyzed during the current study are available from the corresponding author upon reasonable request.

Author Contributions

All authors contributed to the conception and design of the study. Material preparation, data collection and funding acquisition were carried out by Quanwei Cui. The initial and final drafts of the paper were written by Zhongpo Hu, and all authors provided comments on previous versions of the manuscript. All authors have read and approved the final version of the manuscript.

Disclaimer

Publisher's note: Copernicus Publications remains neutral with regard to jurisdictional claims made in the text, published maps, institutional affiliations, or any other geographical representation in this paper. The authors

https://doi.org/10.5194/ms-2026-188
Preprint. Discussion started: 12 November 2026
© Author(s) 2026. CC BY 4.0 License.



mechanical sciences
DISCUSSIONS

bear the ultimate responsibility for providing appropriate place names. Views expressed in the text are those of the authors and do not necessarily reflect the views of the publisher.

Acknowledgments

Funding
The research was supported by the National Natural Science Foundation of China (Grant No. 52505612).

Ethics declarations

Conflict of interest
The author declares that there are no conflicts of interest related to this paper.

References

Alavi, P. S., Rocchi, L., Leppin, C., Molinari, J.-F., and Anciaux, G.: A multiscale model of friction considering the influence of third-body wear particles, Wear, 596, 206719, https://doi.org/10.1016/j.wear.2026.206719, 2026.

Bajpai, P., Kahraman, A., and Anderson, N. E.: A surface wear prediction methodology for parallel-axis gear pairs, J. Tribol., 126, 597–605, https://doi.org/10.1115/1.1691433, 2004.

Blau, P. J., Grejtak, T., and Qu, J.: The characterization of wear-causing particles and silica sand in particular, Wear, 530–531, 204872, https://doi.org/10.1016/j.wear.2023.204872, 2023.

Brandão, J. A., Cerqueira, P., Seabra, J. H. O., and Castro, M. J. D.: Measurement of mean wear coeffi cient during gear tests under various operating conditions, Tribol. Int., 102, 61–69, https://doi.org/10.1016/j.triboint.2016.05.008, 2016.

Capozza, R. and Hanley, K. J.: Wear at an incipient ploughing-cutting transition, Wear, 546–547, 205354, https://doi.org/10.1016/j.wear.2024.205354, 2024.

Dong, N., Cui, Q., Zhou, J., Tong, R., Wang, H., and Lu, F.: Study on wear evolution of spur gears considering dynamic meshing stiffness, J. Mech. Sci. Technol., 37, 3393–3408, https://doi.org/10.1007/s12206-023-0606-3, 2023.

Esteves, P. J., Seriacopi, V., de Macêdo, M. C. S., Souza, R. M., and Scandian, C.: Combined effect of abrasive particle size distribution and ball material on the wear coefficient in micro-scale abrasive wear tests, Wear, 476, 203639, https://doi.org/10.1016/j.wear.2021.203639, 2021.

Feng, K., Ji, J. C., Ni, Q., and Beer, M.: A review of vibration-based gear wear monitoring and prediction techniques, Mech. Syst. Signal Process., 182, 109605, https://doi.org/10.1016/j.ymssp.2022.109605, 2023.

Flodin, A. and Andersson, S.: Simulation of mild wear in spur gears, Wear, 207, 16–23, https://doi.org/10.1016/S0043-1648(96)07467-4, 1997.

Garcia-Suarez, J., Brink, T., and Molinari, J.-F.: Roughness evolution induced by third-body wear, Tribol. Lett., 72, 37, https://doi.org/10.1007/s11249-024-01833-9, 2024.

He, Z., Hu, Y., Zheng, X., and Yu, Y.: A calculation method for tooth wear depth based on the finite element method that considers the dynamic mesh force, Machines, 10, 69, https://doi.org/10.3390/machines10020069, 2022.

Lan, P., Polychronopoulou, K., Zhang, Y., and Polycarpou, A. A.: Three-body abrasive wear by (silica) s and of advanced polymeric coatings for tilting pad bearings, Wear, 382–383, 40–50, https://doi.org/10.1016/j.wear.2017.04.002, 2017.

Liu, M., Bayer, G., Reimers, M., Schünemann, W., König, F., Jacobs, G., Schelenz, R., Bader, N., Poll, G., and Marian, M.: Towards lifetime lubrication of wind turbine gearboxes: Technical and physical investigations on used oils, Wear, 571, 205760, https://doi.org/10.1016/j.wear.2025.205760, 2025.

Qin, C., He, S., Zhou, X., Li, Q., Li, Q., and Yang, Z.: Research on the effect of nano/micron SiO2 particles on actual wear of the main gear box of large-scale mechanical equipment, Tribol. Lett., 72, 12, https://doi.org/10.1007/s11249-023-01814-4, 2024.

Qin, K., Zhou, Q., Zhang, K., Feng, Y., Zhang, T., Zheng, G., Xia, B., and Liu, B.: Non-uniform abrasive particle size effects on friction characteristics of FKM O-ring seals under three-body abrasion, Tribol. Int., 136, 216–223, https://doi.org/10.1016/j.triboint.2019.03.051, 2019.

Ren, J. and Yuan, H.: A dynamic wear prediction model for studying the interactions between surface wear and dynamic response of spur gears, Coatings, 12, 1250, https://doi.org/10.3390/coatings12091250, 2022.

Sainsot, P., Velex, P., and Duverger, O.: Contribution of gear body to tooth deflections—a new bidimensional analytical formula, J. Mech. Des., 126, 748–752, https://doi.org/10.1115/1.1758252, 2004.

https://doi.org/10.5194/ms-2026-188
Preprint. Discussion started: 12 November 2026
© Author(s) 2026. CC BY 4.0 License.



mechanical sciences
DISCUSSIONS

638 Walker, J., Mohammadpour, M., Theodossiades, S., Bewsher, S. R., Offner, G., Bansal, H., Leighton, M.,
639 Braunstingl, M., and Flesch, H.-G.: A multi-physics transient wear model for helical gear pairs, Tribol. Int., 169,
640 107463, https://doi.org/10.1016/j.triboint.2022.107463, 2022.

641 Wu, S., Zuo, M. J., and Parey, A.: Simulation of spur gear dynamics and estimation of fault growth, J. Sound Vib.,
642 317, 608–624, https://doi.org/10.1016/j.jsv.2008.03.038, 2008.

643 Xie, C., Hua, L., Han, X., Lan, J., Wan, X., and Xiong, X.: Analytical formulas for gear body-induced tooth
644 deflections of spur gears considering structure coupling effect, Int. J. Mech. Sci., 148, 174–190,
645 https://doi.org/10.1016/j.ijmecsci.2018.08.022, 2018a.

646 Xie, C., Hua, L., Lan, J., Han, X., Wan, X., and Xiong, X.: Improved analytical models for mesh stiffness and
647 load sharing ratio of spur gears considering structure coupling effect, Mech. Syst. Signal Process., 111, 331–347,
648 https://doi.org/10.1016/j.ymssp.2018.03.037, 2018b.

649 Xing, M., Zhou, C., Li, Y., and Zheng, M.: Wear prediction considering dynamic load for spur gear in
650 mixed elastohydrodynamic lubrication, Proc. Inst. Mech. Eng. Part J-J. Eng. Tribol., 237, 645–654, https:/
651 /doi.org/10.1177/13506501221134998, 2023.

652 Xu, R., Sheng, W., Zhou, F., and Persson, B. N. J.: Rubber wear: History, mechanisms, and perspectives, Tribol.
653 Lett., 73, 90, https://doi.org/10.1007/s11249-025-02025-9, 2025.

654 Yan, L., Guan, L., Wang, D., and Xiang, D.: Application and prospect of wear simulation based on ABAQUS: A
655 review, Lubricants, 12, 57, https://doi.org/10.3390/lubricants12020057, 2024.

656 Yuan, W., Wang, H., Guo, Q., Wang, W., Zhu, Y., Yu, J., and Yang, X.: Study on wear mechanism of helical gear
657 by three-body abrasive based on impact load, Materials, 15, 4135, https://doi.org/10.3390/ma15124135, 2022.

658 Zhang, J., Zhou, J., Wu, A., Cui, Q., and Dong, N.: Lifecycle wear prediction of spur gears with time-d
659 ependent Archard model and surface topography evolution, Results Eng., 29, 108495, https://doi.org/10.10
660 16/j.rineng.2025.108495, 2026.